BIOCHEMISTRY
including biophysical chemistry & molecular biology

Article

pubs.acs.org/biochemistry

Clustering and Dynamics of Phototransducer Signaling Domains Revealed by Site-Directed Spin Labeling Electron Paramagnetic Resonance on SRII/HtrII in Membranes and Nanodiscs

Ioan Orban-Glaß,[†,§] Natalia Voskoboynikova,[†,§] Karin B. Busch,[‡] Daniel Klose,[†] Christian Rickert,[†] Wageiha Mosslehy,[†] Friedrich Roder,[∥] Verena Wilkens,[‡] Jacob Piehler,[∥] Martin Engelhard,[⊥] Heinz-Jürgen Steinhoff,[†] and Johann P. Klare*[,†]

[†]Macromolecular Structure Group, Department of Physics, University of Osnabrück, Barbarastrasse 7, 49076 Osnabrück, Germany
[‡]Mitochondrial Dynamics Group, Department of Biology, University of Osnabrück, Barbarastrasse 11, 49076 Osnabrück, Germany
[∥]Biophysics Group, Department of Biology, University of Osnabrück, Barbarastrasse 11, 49076 Osnabrück, Germany
[⊥]Max Planck Institute of Molecular Physiology, Otto-Hahn-Strasse 11, 44227 Dortmund, Germany

Supporting Information

ABSTRACT: In halophilic archaea the photophobic response is mediated by the membrane-embedded 2:2 photoreceptor/-transducer complex SRII/HtrII, the latter being homologous to the bacterial chemoreceptors. Both systems bias the rotation direction of the flagellar motor via a two-component system coupled to an extended cytoplasmic signaling domain formed by a four helical antiparallel coiled-coil structure. For signal propagation by the HAMP domains connecting the transmembrane and cytoplasmic domains, it was suggested that a two-state thermodynamic equilibrium found for the first HAMP domain in *Np*SRII/*Np*HtrII is shifted upon activation, yet signal propagation along the coiled-coil transducer remains largely elusive, including the activation mechanism of the coupled kinase CheA. We investigated the dynamic and structural properties of the cytoplasmic tip domain of *Np*HtrII in terms of signal transduction and putative oligomerization using site-directed spin labeling electron paramagnetic resonance spectroscopy. We show that the cytoplasmic tip domain of *Np*HtrII is engaged in a two-state equilibrium between a dynamic and a compact conformation like what was found for the first HAMP domain, thus strengthening the assumption that dynamics are the language of signal transfer. Interspin distance measurements in membranes and on isolated 2:2 photoreceptor/transducer complexes in nanolipoprotein particles provide evidence that archaeal photoreceptor/-transducer complexes analogous to chemoreceptors form trimers-of-dimers or higher-order assemblies even in the absence of the cytoplasmic components CheA and CheW, underlining conservation of the overall mechanistic principles underlying archaeal phototaxis and bacterial chemotaxis systems. Furthermore, our results revealed a significant influence of the *Np*HtrII signaling domain on the *Np*SRII photocycle kinetics, providing evidence for a conformational coupling of SRII and HtrII in these complexes.

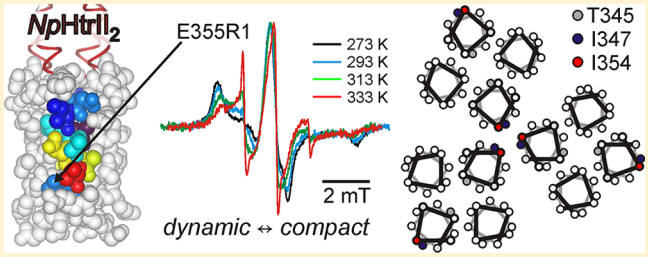

Bacteria as well as halophilic archaea have developed highly similar effective signal transduction systems to receive and process signals from their environment, enabling them to find optimal growth conditions, i.e., seeking nutrients but avoiding harmful substances. In the case of some halophilic archaea, these systems also permit phototaxis in order to seek light of wavelengths matching the absorption maximum of the light driven ion pumps bacteriorhodopsin and/or halorhodopsin but avoid harmful contributions in the UV range.[1] The photophobic response of haloarchaea, such as *Halobacterium salinarum* and *Natronomonas pharaonis*, to harmful blue light is mediated by the membrane-embedded photoactive sensory rhodopsin II (SRII, also known as phoborhodopsin) tightly associated with a cognate transducer protein HtrII (halobacterial transducer of rhodopsin II) (Figure 1A,B). After light activation of SRII, the signal is transferred to HtrII that transmits the signal further to the intracellular two-component pathway which modulates the swimming behavior of the cell. In analogy with the bacterial chemotaxis system (e.g., in enteric bacteria such as *Escherichia coli*), this cytoplasmic signal transduction cascade includes a histidine kinase CheA and the response regulators CheY and CheB (reviewed in, e.g., refs 1−4).

SRII is structurally and functionally related to the light-driven ion pumps bacteriorhodopsin (BR) and halorhodopsin (HR) and consists of seven transmembrane helices (A−G) with a retinal chromophore covalently bound to a conserved lysine

Received: September 13, 2014
Revised: December 6, 2014
Published: December 9, 2014

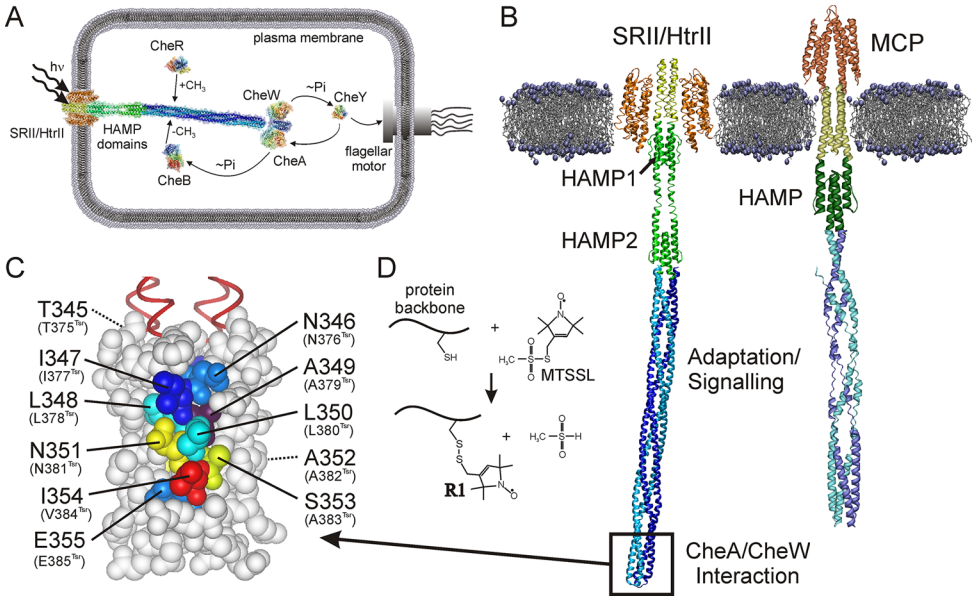

Figure 1. The phototactic system. (A) Two component phosphor-transfer system. Light activation of the photoreceptor *Np*SRII triggers activation of the phototransducer *Np*HtrII. The signal is transferred to the cytoplasmic tip of the molecule, where it modulates the activity of the homodimeric histidine kinase CheA bound together with the adaptor protein CheW. The phosphate group is transferred from CheA to the response regulator/aspartate kinase CheY that functions as a switch for the flagellar motor. The phosphate can also be transferred to the methylesterase CheB that, together with the methyltransferase CheR, mediates adaptation to constant level of stimuli. (B) Models of the *Np*SRII/*Np*HtrII complex from *N. pharaonis* (left) and a eubacterial chemoreceptor (MCP, right) showing the architecture of the protein family. The photoreceptor *Np*SRII and the ligand binding domain in the chemoreceptor are shown in orange. The HAMP domain(s), two in NpHtrII and one in the chemoreceptor, are shown in green. The cytoplasmic signaling/adaptation domains are depicted in blue/cyan. (C) Structure of the NpHtrII CheA/CheW interaction domain indicating positions that have been labeled with MTSSL. (D) Site directed spin labeling. After site-directed mutagenesis to replace the residue of interest by cysteine, reaction of the MTSSL with the sulfhydryl group of the cysteine yields the spin label side chain commonly abbreviated as R1.

residue on helix G via a protonated Schiff base.[5−7] Photoexcitation of SRII induces a photoreaction cycle similar to that of BR.[8] In analogy to the BR photocycle, the intermediates are named K, L, M, N, and O.

The transducer protein HtrII consists of a membrane-embedded N-terminal domain with two transmembrane α-helices, TM1 and TM2, and an elongated α-helical coiled coil cytoplasmic adaptation and signaling domain (Figure 1B). As bacterial chemoreceptors, HtrII forms homodimers (see Figure 1B) and is in membranes tightly bound to SRII with a stoichiometry of 2:2. Thereby, two receptor molecules flank a transducer dimer. Transmembrane and cytoplasmic domains of the transducer are connected by a linker region containing two HAMP (histidine kinase, adenylate cyclase, methyl accepting protein, phosphatase) domains that have been identified in a variety of protein families.[9] The succeeding HAMP domains exhibit a four helical, parallel coiled coil structure with an unusual interhelical packing.[10] The cytoplasmic domain is suggested to be arranged in an antiparallel four helical bundle of two helical hairpins (Figure 1C).[7,11]

Previous site-directed spin labeling (SDSL) electron paramagnetic resonance (EPR) spectroscopy studies[4,11,12] suggested that transduction of the signal in the *N. pharaonis* receptor/transducer (*Np*SRII/*Np*HtrII) complex is triggered by a light-induced movement of helix F, which in turn induces a rotary/screw-like motion of the transducer helix TM2. Detailed SDSL EPR studies further revealed that the first *Np*HtrII HAMP domain (HAMP1), directly succeeding TM2, is engaged in a "two-state" equilibrium between a highly dynamic (dHAMP) and a compact (cHAMP) conformation.[13] This equilibrium was found to be dependent on salt concentration (*N. pharaonis and H. salinarum* are halophiles) and temperature. Time-resolved EPR spectroscopy revealed light-induced changes in the dynamics of a spin label bound to the first HAMP domain that are in line with a transient immobilization in accordance with a shift of the two-state equilibrium toward the compact HAMP conformation.[14] Consequently, a compact HAMP1 structure would characterize the "kinase-on" state. Likewise, Cryo-electron microscopy data for the *E. coli* aspartate chemoreceptor Tar show a "compact" and an "extended" HAMP conformation in receptor trimers-of-dimers, the former corresponding to the "kinase-on" state.[15] However, how the signal is transmitted through the HAMP domain(s) and along the adaptation/signaling domain down to the bound kinase CheA is still subject of discussion.

Bacterial chemoreceptors form trimers-of-dimers[16−18] that are further organized into well-defined higher order clusters together with CheA and CheW (reviewed, e.g., in ref 19). Several features of the *E. coli* chemotaxis system suggest that chemoreceptors and kinases interact in a cooperative manner within these arrays. Amplification factors of at least 50-fold and Hill coefficients up to 10 have been reported, and cooperation between neighboring receptors has been shown to be necessary for precise functioning of sensory adaptation,[19] indicating that receptor clustering in allosterically coupled arrays determines most of the notable features of the signaling system. Although corresponding information about the phototactic systems of archaea is sparse, the striking similarities between the two systems on the level of the components constituting the system and most compellingly the functionality of photoreceptor/transducer-chemoreceptor chimeras[20] strongly suggest that phototaxis receptor/transducer units also cluster in functional arrays. However, the notion that ordered clustering takes place,

dx.doi.org/10.1021/bi501160q | *Biochemistry* 2015, 54, 349−362

as well as a possible dependence of SRII/HtrII function on oligomerization, is yet to be proven.

Here, we investigate the dynamic and structural properties of the cytoplasmic tip domain of *Np*HtrII in terms of signal transduction and putative oligomerization using SDSL EPR spectroscopy. In addition to reconstitution of the proteins in membranes formed by purple membrane lipids (PML), we inserted the *Np*SRII/*Np*HtrII complex into nanolipoprotein particles (NLPs) formed by human apolipoprotein AI (ApoAI) and PML to study the operation of the 2:2 photoreceptor/transducer complex as a "building block" of the archaeal signaling chain. A similar approach has been already used for studying isolated chemoreceptor dimers and trimers-of-dimers[21−23] and recently also for a SRII-HtrII fusion protein.[24]

MATERIALS AND METHODS

Protein Expression and Purification. For purification purposes, all proteins had a C-terminal 6xHis-tag. *Np*SRII-His and the respective cysteine mutants of $NpHtrII_{157}$−His (transducer construct that was truncated at position 157) and *Np*HtrII-His (full-length transducer) (see Figure 1) were expressed in *E. coli* BL21 (DE3) according to refs 25−27 with minor modifications. In brief, cells were grown in LB medium (with 50 mg/mL kanamycin, 37 °C) to an optical density OD_{578} of 0.8−1.0. Overexpression was induced by 0.5 mM IPTG. After induction, cells were incubated for 4 h at 37 °C. Cells were harvested (15 min, 5000 rpm, SLA-3000), 1× washed and then resuspended in cell wash buffer (150 mM NaCl, 25 mM NaP_i, 2 mM EDTA, pH 8.0; 1/100 culture volume) and disrupted by sonication (Branson Sonifier 250). The membrane fraction was isolated by centrifugation (1.5 h, 20.500 rpm, SS34) and membrane proteins solubilized overnight (4 °C) in buffer A (300 mM NaCl, 50 mM NaP_i, pH 8.0, 2% (w/v) *n*-dodecyl-*β*-D-maltoside (DDM)). Solubilized membrane proteins were isolated by centrifugation (1.5 h, 20.500 rpm, SS34) and incubated for 2 h with equilibrated (buffer B: 300 mM NaCl, 50 mM NaP_i, pH 8.0, 0.05% (w/v) DDM) Ni-NTA superflow (Quiagen) material in the presence of 15 mM imidazole. Unspecifically bound proteins were removed by washing with buffer B containing 30 mM imidazole. The His-tagged transducer proteins were eluted with buffer B containing 200 mM imidazole. From the fractions containing the desired protein imidazole was removed by dialysis against 500 mM NaCl, 10 mM Tris pH 8.0, 0.05% (w/v) DDM. If not used directly for spin labeling and reconstitution, protein solutions were stored at −80 °C.

Reconstitution of the NpSRII/NpHtrII Complex into NLPs. NLPs were assembled in vitro according to a protocol adapted from ref 28. The assembly was performed in buffer R (10 mM Tris, pH 8.0, 150 mM NaCl, 5 mM DDM). For reconstitution of the complex, polar lipids from *H. salinarum* and apoA-I were added to the purified, DDM-solubilized *Np*SRII/*Np*HtrII complex. For preparation of the complex, *Np*HtrII was mixed with *Np*SRII in a 1:1 molar ratio and incubated for 12 h at 4 °C. The final concentrations of the components were 0.76 mM lipids, 14 μM apoA-I and 7 μM *Np*SRII/*Np*HtrII. After incubation for 1−2 h at room temperature, the assembly mixture was subjected to SM-2 Bio-Beads (Bio-Rad, Hercules, CA, US) to remove DDM (50 mg of beads/mg of detergent). Bio-Beads were prewashed extensively with methanol and water. Any aggregates were removed by centrifugation at 12000*g* for 15 min at 4 °C. Samples were stored at 4 °C until further use.

Spin Labeling. The spin label (1-oxyl-2,2,5,5-tetramethylpyrroline-3-methyl) methanethiosulfonate (MTSSL; Enzo life sciences, NY) was covalently attached to the cysteine residues of both *Np*HtrII-His and $NpHtrII_{157}$−His mutants solubilized in DDM as described previously.[13] In brief, the protein was incubated with 10 mM dithiothreitol (overnight) and then dialyzed against 500 mM NaCl, 10 mM Tris pH 8.0, 0.05% (w/v) DDM to remove the reduction agent. Afterward the protein was incubated overnight with 1 mM MTSSL, and excess label was removed by repeated dialysis. In the following the spin labeled cysteine residue is abbreviated as R1. Single site labeling of *Np*HtrII results in the introduction of two symmetry-related spin labels in the transducer dimers and allows for the detection of additional spin−spin interactions in higher oligomers.

Electron Paramagnetic Resonance Spectroscopy. Continuous wave (cw) EPR spectra were recorded at room temperature (296−299 K) with a homemade EPR spectrometer equipped with a Bruker dielectric resonator, with the microwave power set to 0.4−0.6 mW and B-field modulation amplitude adjusted to 0.15 mT. Samples were loaded into EPR glass capillaries (0.9 mm inner diameter) at final protein concentrations of 15−20 μM (sample volume 15 μL). For temperature-dependent cw EPR measurements the X-band EPR spectrometer mentioned before was used in combination with a liquid flow cryostat (30% ethylene glycole, 70% water) to adjust the sample temperature in the range 263−333 K.

Low temperature cw EPR spectra for interspin distance determination in the range from ∼8 to 25 Å were obtained on a homemade cw X-band EPR spectrometer equipped with a Super High Sensitivity Probehead (BrukerBiospin GmbH, Germany). The magnetic field was measured with a RMN-2 B-field meter (Drusch GmbH, Germany). A continuous flow cryostat Oxford ESR900 (Oxford Instruments, UK) was used in combination with an Intelligent Temperature Controller ITC 4 (Oxford Instruments, UK) allowing the stabilization of the sample temperature to 160 K. The microwave power was set to 0.2 mW and the B-field modulation amplitude to 0.25 mT. EPR quartz capillaries (3 mm inner diameter) were filled with sample volumes of 40 μL. Fitting of simulated dipolar broadened EPR powder spectra to the experimental ones detected at 160 K was carried out as described before in detail.[29]

DEER measurements were carried out at X-band frequencies (9.3−9.4 GHz) with a Bruker Elexsys 580 spectrometer equipped with a Bruker Flexline split-ring resonator ER 4118XMS3 and a continuous flow helium cryostat ESR900 (Oxford Instruments) controlled by an Oxford Intelligent temperature controller ITC 503S. Measurements were performed using the four-pulse DEER sequence:[30,31]

$$\pi/2(\nu_{obs}) - \tau_1 - \pi(\nu_{obs}) - t' - \pi(\nu_{pump}) - (\tau_1 + \tau_2 - t') - \pi(\nu_{obs}) - \tau_2 - \text{echo}$$

A two-step phase cycling $(+\langle x\rangle, -\langle x\rangle)$ was performed on $\pi/2$ (ν_{obs}). Time t' was varied, whereas τ_1 and τ_2 were kept constant. The dipolar evolution time is given by $t = t' - \tau_1$. Data were analyzed only for $t > 0$. The resonator was overcoupled to $Q \approx 100$; the pump frequency ν_{pump} was set to the center of the resonator dip and coincided with the maximum of the nitroxide EPR spectrum, whereas the observer frequency ν_{obs} was ∼65 MHz higher, coinciding with the low field local maximum of the spectrum. All measurements were performed at a temperature of 50 K with observer pulse lengths

dx.doi.org/10.1021/bi501160q | *Biochemistry* 2015, 54, 349−362

of 16 ns for $\pi/2$ and 32 ns for π pulses and a pump pulse length of 12 ns. Proton modulation was averaged by adding traces at eight different τ_1 values, starting at $\tau_{1,0}$ = 200 ns and incrementing by $\Delta\tau_1$ = 8 ns. Data points were collected in 8 ns time steps. The total measurement time for each sample was 8−24 h. Data analysis was performed with DeerAnalysis2011/2013.[32]

Thermodynamic Analysis of the Temperature Dependency of the cw EPR Spectra. Fitting of simulated EPR spectra to the experimental ones detected in the temperature range from 263 to 333 K was performed using a simple Brownian model of isotropic reorientational diffusion of the nitroxide side chain.[33] The spectra were fitted with two distinct spectral components. The rotational diffusion constants R and the ratio of the two spectral components were allowed to vary with temperature. The reorientational correlation time τ_c was calculated from the obtained rotational diffusion constant R as $\tau_c = (6 \times R)^{-1}$. It should be noted that simulation of the component characterized by longer correlation times (immobilized component, i) must be considered strongly approximated due to the inherent more complex influence of reorientational potentials in determining the spectral shape.

The enthalpy of activation for the reorientational motion of the nitroxide was obtained by linear interpolation of log (τ_c) versus $1/T$ (Arrhenius plots), and the natural logarithm of the variation of the component ratio with temperature ($K_{eq} = f_{mobile}/f_{immobile}$) versus $1/T$ (van't Hoff plots) provides the reaction entropy and enthalpy values determined from the intercept and slope of the regression line according to the equation $\ln K_{eq} = -(\Delta H/RT) + (\Delta S/R)$, respectively.

Rotamer Library Analysis. In the rotamer library approach (RLA) the canonical ensemble of possible spin label side chain conformations is modeled by a discrete set of 210 precalculated rotamers.[34] From the RLA a conformational distribution of the spin label side chain at any chosen position in the otherwise fixed protein structure can be determined as described in detail in ref 34. In brief, the superposition of the spin label side chain's backbone atoms onto the protein backbone at the respective position provides the orientation of the label side chain with respect to the protein structure and allows to calculate a resulting energy for the spin label-protein interaction from the Lennard-Jones potential using the MD force field CHARMM27.[35] Subsequent Boltzmann weighting and normalization by the partition function yields a probability for each rotamer which is then multiplied by the probability of the spin label side chain to exhibit each conformation. This results in the final rotamer probability distribution at the site of interest. Between two such probability distributions at two positions in the protein, a distance distribution is calculated as the histogram of all pairwise interspin distances weighted by the product of their respective probabilities.

Size-Exclusion Chromatography (SEC). The column (Superdex 200 10/200 GL, GE Healthcare) was run at a flow rate 0.5 mL/min on an ÄKTA FPLC system (GE Healthcare) at 8 °C. Calibration of the column was carried out with a mixture of proteins of known size.

Transmission Electron Microscopy Imaging. For transmission electron microscopy imaging (TEM), samples containing reconstituted NLPs (5 μL) were placed for 1 min on Formvar coated single slot copper grids (Agar Scientific, Stansted, England). The grid was tapped with filter paper to remove surface water and then air-dried. Electron micrograph images were recorded with a transmission electron microscope Zeiss EM 902 A (Carl Zeiss, Jena, Germany) operated at 50 kV. Particles sizes were measured from the micrographs using ImageJ (National Institutes of Health, Bethesda, Maryland, US).

Fluorescence Labeling. Fluorescence labeling of cysteine mutants of *Np*HtrII with maleimide functionalized Alexa Fluor 488 (Alexa 488), Alexa Fluor 594 (Alexa 594) and ATTO 655 at Cys350 (see Figure 1) was carried out according to the manufacturer's protocol.

Fluorescence Cross-Correlation Spectroscopy Analysis. Fluorescence cross-correlation spectroscopy analysis (FCCS) experiments were carried out with an Olympus Fluoview 1000 microscope equipped with a dual channel fluorescence lifetime upgrade kit from Picoquant. Pulsed laser diodes at 485 and 640 nm were used to excite Alexa 488 and ATTO 655, respectively, through a 60x/1.2NA water immersion objective. A 525/50 nm emission filter was used for the green channel and a 690/70 nm filter for the red channel.

Single Molecule Imaging. For single molecule (SM) recording, samples were mounted on an inverse microscope Olympus (IX71 and 60× oil objective (Olympus Planapo N.A. 1.45)) equipped with a TIRF-condensor (Olympus). Excitation of Alexa 594 was provided by a solid state laser (561 nm, 200 mW). Alexa 488 was excited by an argon−Krypton laser (488 nm, 250 mW). Images were captured by a back-illuminated EMCCD camera (Andor iXON 897) with an image capture frequency of 20 Hz.

Flash Photolysis. Transient optical absorption experiments were carried out as described previously.[36] A 50 W halogen lamp with an infrared cutoff filter (KG-2) and 400 nm, 500 or 550 nm interference filters, respectively, illuminated the sample-filled quartz cuvette inside a sample holder temperature-controlled to 298 K. The transmitted light was passed through a monochromator and detected with a photodiode. A flashlight with a flash duration of 80 μs equipped with a 475 nm edge filter provided excitation perpendicular to the transmission beam. The amplified signal was recorded with an analog-to-digital converter connected to a standard PC. For the transitions between the late photocycle intermediates (t > 2 ms) studied here, the kinetics determined by flashlight excitation were indistinguishable from those determined by pulsed laser excitation. The transient absorption changes were recorded at 25 °C on samples buffered in 10 mM Tris, pH 8.0, 500 mM NaCl at concentrations of approximately 5 μM.

RESULTS AND DISCUSSION

Eleven succeeding residues (T^{345}NILALNASIE^{355}, Figure 1C) one helical turn above the short loop at the end of the transducer bundle were mutated to cysteines one by one and subsequently coupled to the methanethiosulfonate spin label (MTSSL, Figure 1D) to yield the nitroxide side chain R1. The spin labeled mutants, reconstituted together with the photoreceptor in a 1:1 molar ratio into PML, have been investigated in terms of the mobility of the R1 side chain in dependence of salt concentration and temperature, and distances between spin labels in transducer dimers and putative trimers-of-dimers or higher oligomers.

Effects of Viscosity, Ionic Strength, and Protein/Lipid Ratio on the NpHtrII Tip Domain. The room temperature X-band EPR spectra recorded for the spin-labeled residues in the *Np*SRII/*Np*HtrII complex reconstituted in PML in 500 mM or 3.3 M NaCl are presented in Figure 2. Replacement of

dx.doi.org/10.1021/bi501160q | *Biochemistry* 2015, 54, 349−362

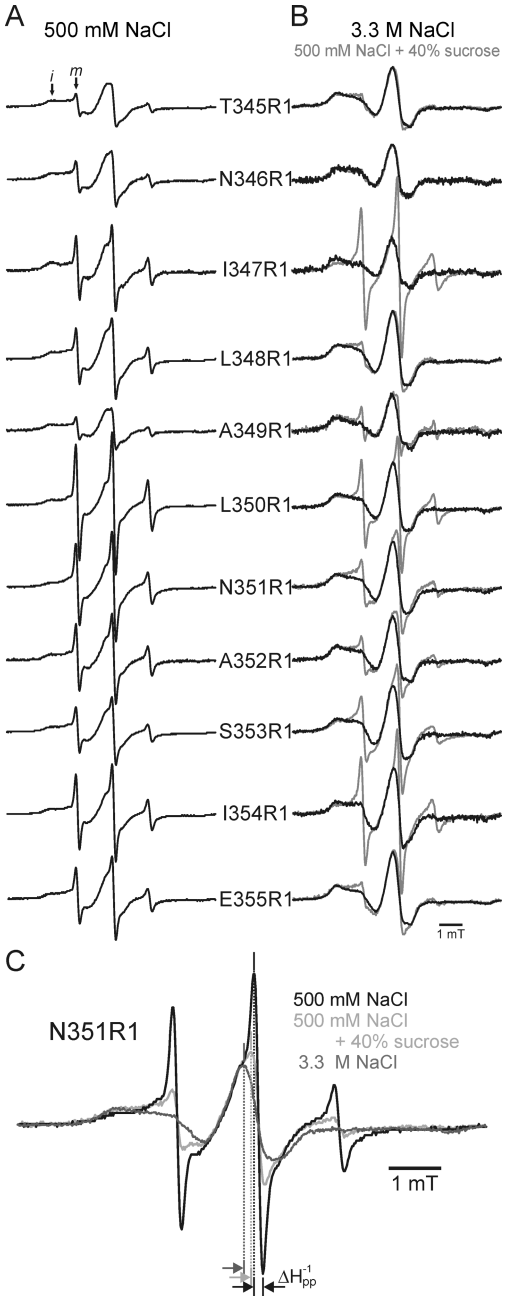

Figure 2. Dependence of spin label mobility on viscosity and salt concentration. EPR spectra for selected positions in NpSRII/NpHtrII reconstituted in PML detected at low salt concentration (500 mM NaCl, panel A) and at high ionic strength (3.3 M NaCl, panel B, black) or in 40% sucrose (+500 mM NaCl; panel B, gray). For sake of comparison, some of the spectral amplitudes were multiplied by scaling factors. (C) Enlarged view on the spectra for NpHtrII-N351R1.

sodium by potassium ions does not lead to significant spectral changes (data not shown). The majority of the EPR spectra present a composite spectral shape, revealing the presence of at least two components related to mobile (m) and immobile (i) fractions of the spin label side chain. The term "mobility" is used here in a general sense and includes effects on the spectral line shape due to the motional rate, the amplitude, and the anisotropy of the nitroxide side chain reorientation. These parameters characterize the motional freedom of the spin label in the nanosecond time scale. The more immobile spectral component (i) can be approximately simulated with an effective isotropic reorientational correlation time of about 200 ns. The mobile component (m), exhibiting a narrow three line spectrum, is characterized by correlation times <5 ns. The correlation times for the mobile component fall below that observed for highly dynamic loop regions,[37] suggesting that protein backbone fluctuations must be involved in determining the fast dynamics of the nitroxide side chain.

In general, the presence of two spectral components characterized by different mobilities could result from structural constraints in the microenvironment of the spin label, leading to different stable spin label side chain conformations or different protein conformations in equilibrium.[38,39] Because (i) the spectra for all label positions show at least two components, (ii) it appears unlikely that similar local structural constraints leading to distinct spin label conformations exist for all 11 positions investigated here, and (iii) similar observations have been made for all cytoplasmic positions in *Np*HtrII investigated so far in the first HAMP domain[13,24,40] as well as in the inter-HAMP region and the second HAMP domain (unpublished data), we conclude that the *Np*HtrII tip domain is also involved in a protein conformational equilibrium at room temperature. Noteworthy, in vitro as well as in vivo studies on the SRI/HtrI complex from *H. salinarum* also suggested a two-state model for signal transduction, where one state activates CheA whereas the other conformation inhibits the kinase.[41,42]

Increasing the salt concentration from 500 mM to 3.3 M NaCl, close to the physiological salt concentration,[43,44] led to an almost complete suppression of the mobile component (m) for all positions investigated. This is most evident for variants displaying a distinct mobile component (e.g., see residues I347R1, L350R1, and I354R1 in Figure 2). The fraction of the dynamic component is generally suppressed at high salt concentrations. Also this behavior resembles that observed for *Np*HtrII variants spin labeled in the HAMP domains(s).

An additional influence of the viscosity of the surrounding buffer solution on the spectral changes detected was investigated by recording spectra at 500 mM NaCl concentration in the presence of sucrose (40% w/v, viscosity $\eta_{40\%\ \mathrm{sucrose}}$ = 6.2 cP, Figure 2B, gray spectra). For comparison, the viscosity of water at 293 K is 1.002 cP, and that of a saturated salt solution $\eta_{4\ \mathrm{M\ NaCl}}$ = 1.6 cP.[45] Despite the fact that the increase in viscosity induced by 40% sucrose is ∼12 times larger than that induced by high salt concentrations, the salt-induced spectral effects are observed to be most pronounced. Thus, it can be excluded that the spectral changes observed for the *Np*HtrII tip are solely viscosity-caused.

The spin label side chain mobility was quantified via the inverse line width of the central resonance line, ΔH_{pp}^{-1} (Figure 3). At low salt concentration remarkably high mobility values of 5.5 ± 1.0 mT^{-1} are observed, in line with the dominating mobile spectral component and being indicative for a highly dynamic structure. A periodic pattern in the values of the mobility parameter compatible with an α-helical structure is visible only up to position 349. Although increased viscosity of the solution significantly reduces the overall mobility (ΔH_{pp}^{-1} = 3.5 ± 1.5 mT^{-1}) and seems to promote a helical structure only at physiological salt concentration (3.3 M NaCl) the mobility plot reveals a clear α-helical periodicity in the values of the inverse line width of ∼3.6 residues, suggesting that the four-helix bundle structure of the cytoplasmic tip is stabilized under this condition. Indeed, it seems that the two spectral components characterize a dynamic and a rigid or compact α-helical coiled coil structure in thermodynamic equilibrium. At

dx.doi.org/10.1021/bi501160q | *Biochemistry* 2015, 54, 349−362

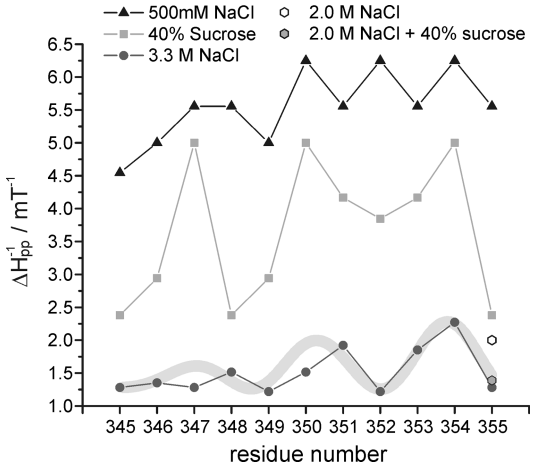

Figure 3. Spin label mobility analysis for the receptor-transducer complex (*Np*SRII-*Np*HtrII) reconstituted in PML. Mobility parameters ΔH_{pp}^{-1} obtained from the cw RT EPR spectra (Figure 2) in 500 mM NaCl (black triangles), 500 mM NaCl + 40% sucrose (gray squares), and 3.3 M NaCl (black circles). For *Np*SRII/*Np*HtrII-E355R1 in addition the mobility parameter has been determined for samples in buffer with 2 M NaCl (open hexagon) and 2m NaCl + 40 sucrose (gray filled hexagon) to seek for conditions suitable for cw distance measurements at 160 K (see text). The bold gray line depicts the periodicity of an α-helix.

low salt concentration, this equilibrium is on the side of the dynamic state, whereas at high (physiological) salt concentration the rigid/compact state seems to prevail. Remarkably, the low mobility values observed at 3.3 M NaCl (ΔH_{pp}^{-1} = 1.7 ± 0.5 mT^{-1}) indicate the presence of secondary/tertiary interactions of the nitroxide for *all* positions including those that should be oriented toward the aqueous phase according to the structural model based on the high sequence conservation compared to *E. coli* Tsr (see Figure 1C), e.g., positions 347 and 350. Although we cannot safely exclude a structural arrangement of the tip region of *Np*HtrII being different from this model, at least a fraction of the studied spin labeled sites should be surface exposed in an isolated dimer and consequently display significantly higher mobility values than observed. Thus, the observed spin label dynamics in native lipids at physiological salt concentrations suggest that tertiary contacts also exist between multiple *Np*HtrII dimers.

Additional experiments performed on samples with higher lipid content (400-fold instead of 40-fold molar excess of lipids over *Np*SRII/*Np*HtrII, see Supplementary Figure S1, Supporting Information) exhibit no significant spectral differences compared to the samples with low lipid content. Thus, the observed tertiary contacts between *Np*HtrII dimers in PML membranes are not due to the high protein/lipid ratio chosen to optimize the EPR signal strength.

Evaluation of buffer conditions suitable for interspin distance measurements in the frozen state (i.e., reduced salt concentration (2 M NaCl) and addition of sucrose (40%, + 2 M NaCl) as a cryoprotectant) on the mutant E355R1 revealed that an intermediate salt concentration and increased viscosity mimics the 3.3 M NaCl condition almost perfectly.

Temperature Effects on the EPR Spectral Features. For the first HAMP domain of *Np*HtrII, it has already been shown that the presence of two spectral components reflects two conformations—a compact (*c*HAMP) and a dynamic (*d*HAMP) state—in a two-state equilibrium that can be shifted not only by varying salt concentration and temperature, but also by light. Thus, it was concluded that the two conformations represent different signaling states of the transducer.[13,14] To investigate if the two spectral components observed in the EPR spectra of the tip mutants reflect a similar two-state equilibrium as that observed for the HAMP domain(s), we analyzed the temperature dependence of the EPR spectra for selected positions (A349R1, N351R1, I354R1, and E355R1) at 3.3 M NaCl to obtain the thermodynamic parameters according to the method described previously.[40] Selected spectra (A) and the thermodynamic analyses (B) for positions 351 and 355 are shown in Figure 4 (The full sets of

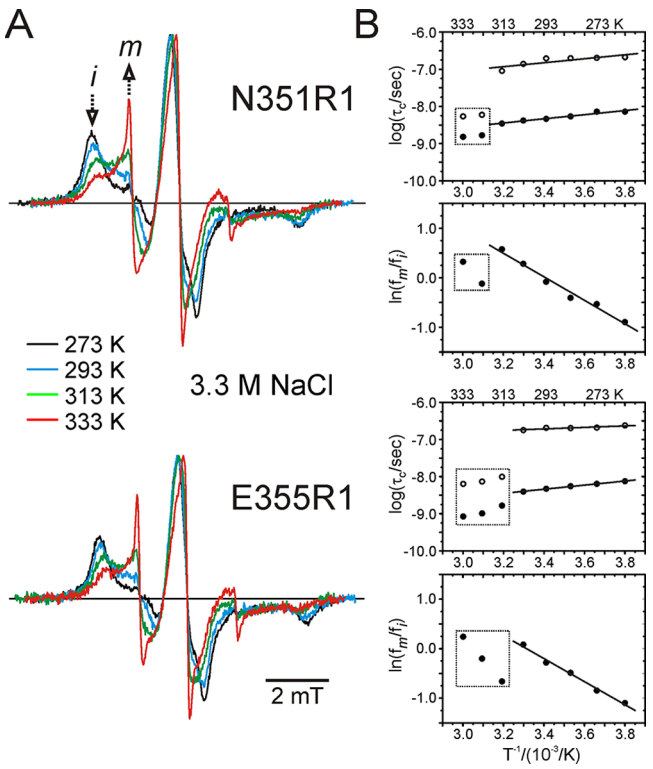

Figure 4. Temperature dependent spectral changes and thermodynamic analyses of reconstituted *Np*SRII/*Np*HtrII-N351R1 and -E355R1. (A) Cw EPR spectra for selected temperatures. Arrows in the upper panel indicate the direction of the spectral changes upon decreasing the temperature. Measurements were performed in the presence of 3.3 M NaCl. (B) Arrhenius (logarithm of the rotational correlation times τ_c (immobile component, open circles; mobile component, filled circles) versus the inverse of the temperature) and van't Hoff plots (natural logarithm of the concentration ratio of the two spectral components, $\ln(f_{mobile}/f_{immobile})$, determined from their second integral versus the inverse of the temperature) for the two positions. Dotted frames indicate data points for which deviation from the linear dependency on the inverse temperature indicates thermal unfolding of the tip domain.

EPR spectra and the Arrhenius and van't Hoff plots for all four positions are given in Supplementary Figure S2, Supporting Information). As obvious from the spectra decreasing the temperature resulted in shifting the equilibrium toward the compact conformation.

The similar slopes of the linear regression lines in the Arrhenius plots for both positions suggest similar activation energies for the reorientational motion of the spin label side chain in both states, and is found to be in agreement with

dx.doi.org/10.1021/bi501160q | *Biochemistry* 2015, 54, 349−362

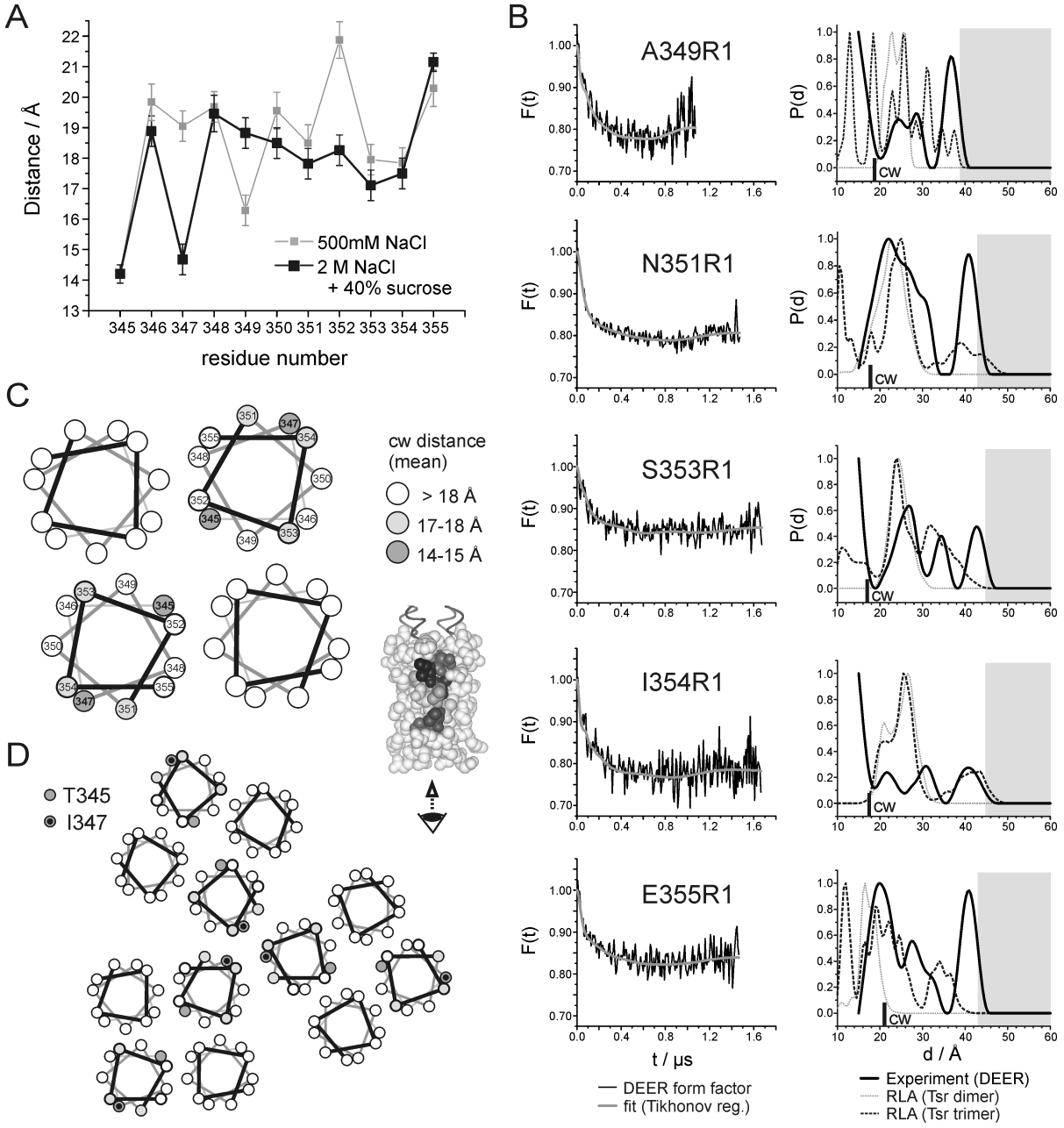

Figure 5. Interspin distance analysis. (A) Mean interspin distances obtained from fitting of simulated dipolar broadened EPR powder spectra to the experimental ones detected at 160 K. (B) DEER background corrected dipolar evolution data (left column) and resulting distance distributions (right column, black solid lines) obtained by Tikhonov regularization of the data shown on the left. The gray dotted and black dashed lines represents the results of a RLA on the Tsr structural model (see Figure 1B,C and panel C in this figure). (C) Helical wheel representation of the *Np*HtrII tip region investigated in this study. Selected interspin distance regimes from the cw experiments (see panel A) are indicated in the scheme (see legend). The tip in this scheme is seen from the bottom of the tip (see inset). (D) Helical wheel representation for a trimer-of-dimer arrangement of the tip region. The schemes in (C) and (D) are based on the crystal structure of the Tsr cytoplasmic domain (pdb: 1QU7).[16] The numbering corresponds to *Np*HtrII (cf. Figure 1C for the relation between the Tsr and *Np*HtrII residue numbers).

previously published data.[13,46] Analyses of the van't Hoff plots reveals the thermodynamic parameters for all positions to be in the same range: ΔH = 17.5−22.0 ± 1.5 kJ/mol, ΔS = 58−73 ± 5 J/mol·K, $\Delta G_{298\ K}$ = 0.1−0.3 ± 3.1 kJ/mol and K_{eq} = 0.9−1.0 ± 0.7 (see Supplementary Figure S2 for details). The agreement of the equilibrium constants throughout the investigated tip positions confirms the assumption that a two-state equilibrium between a dynamic and a compact conformation exists also for the *Np*HtrII tip domain.

Interspin Distance Measurements by cw and Pulsed EPR. The interspin distance analysis performed on the *Np*SRII/*Np*HtrII$_{157}$ complex in PML is presented in Figure 5. Low temperature (160 K) cw X-band EPR spectra of singly spin labeled transducers at low and high salt concentrations were recorded (data not shown) and analyzed in terms of dipolar broadening (see Materials and Methods). For technical reasons the low temperature cw experiments have been carried out with samples in buffer with intermediate salt concentration (2 M NaCl) and 40% sucrose as a cryoprotectant. Such conditions

dx.doi.org/10.1021/bi501160q | *Biochemistry* 2015, 54, 349−362

have been shown (see Figure 3) to lead to the same spectral features at room temperature as observed at 3.3 M NaCl. The mean interspin distances at low and high salt concentration are shown in Figure 5A.

The cw EPR interspin distance analysis (Figure 5A) reveals significant differences between the samples measured with 500 mM NaCl and those with 2 M NaCl and 40% sucrose, again indicating a dependency of the structural features on the environmental conditions. Remarkably, interspin distances < 20 Å are found also for positions in the transducer dimer bundle that are located opposite on a helical wheel (see helical wheel representation in Figure 5C) like positions 345 and 347. Other structural arrangements than that found for Tsr are hardly to envision. The only way to arrange the labeled helices in the dimer with distances between 345R1 and 345R1′ and between 347R1 and 347R1′ less than 15 A, e.g., would unavoidably lead to an even closer contact between 346R1 and 346R1 or between 348R1 and 348R1′, which is not observed. This strongly supports the presence of interdimer contacts for *Np*HtrII in the lipid bilayer as it has been deduced from the mobility analysis.

Additionally, pulse experiments (double electron−electron resonance, DEER) were performed on five selected R1 residues representative for different side chain orientations in the dimer structure (Figure 5C) for which the distances between spin labels are more than 15 Å apart. The results of the DEER distance analysis with the background-corrected dipolar evolution data given in the left column and the distance distributions obtained by Tikhonov analysis from that data in the right column are shown in Figure 5B. In all cases, multimodal distance distributions are obtained that cover the whole interspin distance range from ∼15 to 40−45 Å accessible by the experiment (the upper limit of the accessible distance range depends on the dipolar evolution time and marked by gray boxes in the distance distribution), indicating *multiple* spin spin interactions for all positions in the *Np*HtrII tip investigated by DEER. This finding is independent of the lipid-to-protein ratio as lipid dilution experiments, i.e., decreasing the molar protein:lipid ratio from 1:40 to 1:400, revealed no significant spectral changes upon reduction of the ratio (see Supplementary Figure S1, Supporting Information), supporting that oligomerization of the complex in lipids is driven by protein−protein interactions and not by spatial restrictions. Thus, from the interspin distance analysis performed in this study we conclude that *Np*SRII/*Np*HtrII forms large arrays in the cell membrane like it has been shown for bacterial chemoreceptors. This unequivocally supports the notion already made based on the cw distance measurements that the transducer dimers further oligomerize to form higher order clusters in the membrane. Notably, formation of these clusters takes place in the absence of the CheA/CheW arrays present in cells, resembling the finding that chemoreceptors aggregate through their cytoplasmic domains even in the absence of other chemotaxis proteins.[47]

Inter Spin Distance Simulation in NpHtrII Dimers and Trimers-of-Dimers Based on a Rotamer Library Approach. Chemoreceptor dimers are known to assemble into trimers of dimers (Figure 5D).[16−18] In order to enable comparison between the EPR distance data for *Np*HtrII and such structural models, in silico spin-labeling of the tip positions investigated by DEER was carried out. Simulation of the expected interspin distances was obtained based on a rotamer library approach implemented in the software package MMM.[34] From a set of precalculated spin label side chain conformations, this simulation approach provides those rotamers which can be populated in the structure and predicts the distances between the nitroxide labels at different sites. The results of the simulations are included in the distance distributions in Figure 5B for a transducer dimer (gray, dotted distributions, cf. Figure 5C) and a putative trimer-of-dimers (black, dashed distributions, cf. Figure 5D). Comparison with the experimental data shows that the calculated intradimer distances coincide reasonably well but explain in all cases only parts of the experimental distance distributions. In contrast, if the distances are calculated from the trimer-of-dimer model (Figure 5D) the agreement with the experimental data increases, strongly suggesting that—in analogy to the chemoreceptors like Tsr—also *Np*HtrII forms trimer of dimer assemblies in PML membranes. Moreover, additional or higher populated interspin distance contributions mostly at longer distances in the experimental data for all spin label positions investigated by DEER further indicate the formation of larger arrays.

Incorporation of NpSRII/NpHtrII into Nanolipoprotein Particles (NLPs). The oligomerization of *Np*SRII/*Np*HtrII dimers in PML as revealed above prevents exploration of the functional properties of a single *Np*SRII/*Np*HtrII dimer. Thus, we used a NLP approach to study the operation of the 2:2 photoreceptor/transducer complex as a functional part of the archaeal signal transfer cascade concerning the equilibrium between dynamic and compact conformations of the tip region. Reconstitution of *Np*SRII/*Np*HtrII into NLPs consisting of PML and human full-length apoA-I was carried out at a lipid/apoA-I/2:2 complex molar ratio of 110:2:1.

Size exclusion chromatography (SEC) demonstrated stable species retaining the retinal chromophore by means of monitoring its absorption maximum at 500 nm. As depicted in Figure 6, SEC fractionation of empty NLPs (Figure 6A) and NLPs reconstituted with a *Np*SRII/*Np*HtrII$_{157}$ complex with a transducer truncated right before the second HAMP domain (Figure 6B), results in single elution peaks corresponding to Stokes radii of 45 and 50 Å, respectively. Contrarily, NLPs assembled with *Np*SRII/*Np*HtrII (full-length transducer) exhibit two peaks with Stokes radii of ∼70 and ∼50 Å (Figure 6C). Hence, SEC purification of the *Np*SRII/*Np*HtrII/NLP complex revealed particle size heterogeneity. This phenomenon has been already described for several different self-assembled NLPs.[28,48−51] Moreover, studies employing single-particle techniques such as atomic force microscopy (AFM) and MD simulations revealed a relation between the observed discrete NLPs sizes and changes in the apolipoprotein conformation and/or variations in the number of apolipoproteins per particle, possibly due to the high intrinsic flexibility of the lipoprotein scaffold.[52,53] Hence, the distribution of discrete NLP sizes seems to be a general phenomenon for self-assembled NLPs. Optimal apolipoprotein scaffold/lipid ratios and multiple SEC purification steps might improve the formation of more homogeneous NLP populations. The shape and the structure of assembled NLPs after SEC purification were probed by using single particle TEM imaging. TEM images of assembled NLPs from the peak corresponding to a Stokes radius of 70 Å showed homogeneous populations of well-defined discoidal particles with monodispersed size distribution (Figure 6, D-F).

Stoichiometry of NpSRII/NpHtrII in NLPs. The approximate stoichiometry of the *Np*SRII/*Np*HtrII complex assembled in NLPs can be estimated from absorbance measure-

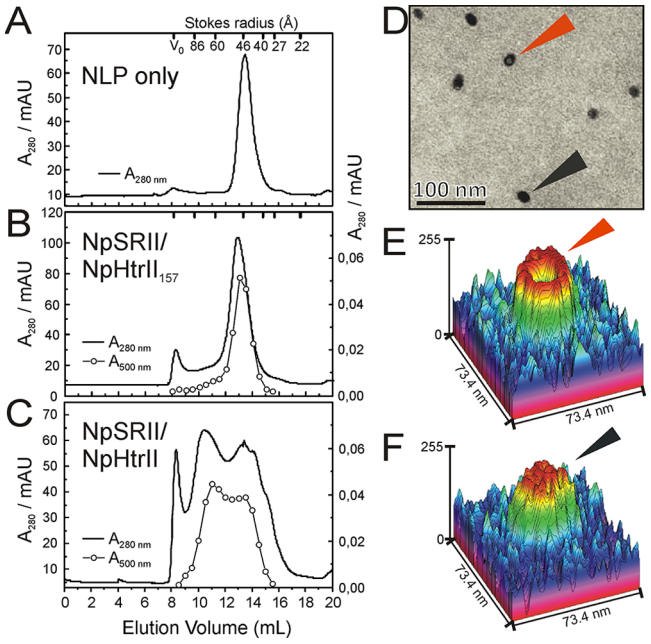

Figure 6. Analysis of the reconstitution of the *Np*SRII/*Np*HtrII complex in NLP by gel filtration and TEM. (A) gel filtration (Superdex 200 10/200 GL) elution profiles for NLPs assembled (top) in the absence of the purified receptor/transducer complex, (center) in the presence of the purified *Np*SRII/*Np*HtrII$_{157}$ or (bottom) in the presence of the purified *Np*SRII/*Np*HtrII complex. Assembly mixtures usually consisted of 14 μM apoA-I and 0.76 mM PML. For receptor/transducer complex reconstitution, either 7 μM *Np*SRII/*Np*HtrII$_{157}$ or 7 μM *Np*SRII/*Np*HtrII were added to the assembly mixture. The calibration of the gel filtration column is given at the top. Protein elution was monitored by absorbance at 280 nm (black solid line) and at 500 nm (black line with open circles). (D) TEM image of *Np*SRII/*Np*HtrII/NLP assemblies shows their homogeneous discoidal shape and monodispersed size distribution. The red arrow points toward an empty NLP and the black arrow points toward a filled NLP indicating two different populations of NLPs. (E, F) High resolution topographical images of an empty NLP and a target-filled NLP, respectively.

ments. The known extinction coefficients of *Np*SRII (at 280 and 500 nm) and apoA-I (at 280 nm) were used to calculate the average *Np*SRII/*Np*HtrII complex: apoA-I molar ratio in the purified NLP preparations after SEC. For the complex with a truncated transducer, *Np*SRII/*Np*HtrII$_{157}$, assembled at a lipid/apoA-I molar ratio of 80:1, the ratio was estimated to be ~0.8, whereas in the presence of the full-length transducer, *Np*SRII/*Np*HtrII, assembled at a lipid/apoA-I ratio of 55:1, the average complex/apoA-I molar ratio was found to be ~1.0. Taking into account that most likely two apoA-I molecules wrap around one NLP,[28,49] these data suggest that one particle contains one *Np*SRII/*Np*HtrII complex with a 2:2 stoichiometry.

To confirm that a single 2:2 *Np*SRII/*Np*HtrII complex was assembled into one NLP, we applied fluorescence cross-correlation spectroscopy (FCCS).[54,55] In this approach the intensity fluctuations of two spectrally separated fluorescent labels are recorded simultaneously by two independent detection channels, which can subsequently be analyzed by using a cross-correlation function. The amplitude of this function reflects the codiffusion of two distinct fluorescent species and thus indicates their association in the same complex.[54,56−58]

Here, *Np*HtrII was labeled either with Alexa 488 or ATTO 655 or with an equimolar mixture of both dyes at position 350 (see Figure 1). Fluorescently labeled *Np*HtrII was then reconstituted together with *Np*SRII into NLPs and fractionated by SEC. For FCCS analysis, again the NLP fraction from the peak corresponding to a Stokes radius of ~70 Å was taken. Figure 7A shows the autocorrelation curves for each of the two channels and the cross-correlation between the two channels obtained from samples containing *Np*HtrII labeled only with Alexa 488 or only with ATTO 655 that have been mixed *after* reconstitution into NLPs. Under these conditions, no cross-correlation was observed. In contrast, significant cross-

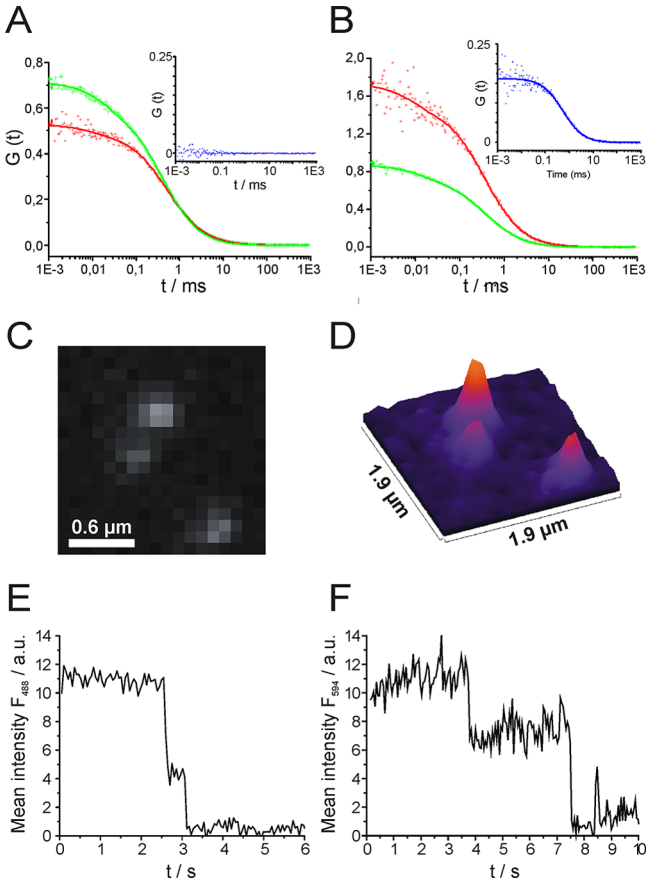

Figure 7. Analysis of *Np*SRII/*Np*HtrII/NLP assemblies by cross correlation fluorescence spectroscopy and single molecule microscopy. (A, B) Autocorrelation and cross-correlation curves were recorded from (A) an equimolar mixture of two NLP fractions containing *Np*HtrII labeled with Alexa 488 or with ATTO 655; (B) a NLP fraction where *Np*HtrII is labeled with mixture of both dyes. Green dots: autocorrelation of Alexa 488. Red dots: autocorrelation of ATTO 655. The insets show a cross-correlation function between *Np*HtrII-Alexa 488 and *Np*HtrII-ATTO 655 (blue dots). Solid lines: fitting functions. (C) TIRF-image (1.9 μm^2) of single *Np*HtrII-Alexa 488 emitters in *Np*HtrII/*Np*SRII/NLP assemblies. (D) Integrated intensities as a surface plot diagram of the same emitters demonstrate the broadening of the punctual signals due to optical diffraction and the pixelated imaging. (E) Fluorescence time trace of the *Np*HtrII/*Np*SRII/NLP complex containing *Np*HtrII labeled with Alexa 488. The particle contains two fluorescent *Np*HtrII molecules as seen by the bleaching in two distinct steps. (F) Fluorescence intensity plot over time from a single complex containing two Alexa 594-labeled *Np*HtrII-molecules. The emitters bleach subsequently in a two-step process. Scales: Pixel size = 0.105 μm, 20 Hz.

dx.doi.org/10.1021/bi501160q | *Biochemistry* 2015, 54, 349−362

correlation was obtained for *Np*HtrII labeled with a 1:1 mixture of the dyes *before* reconstitution into NLPs (Figure 7B). Quantitative analysis showed that 37.5% of the ATTO 655-labeled *Np*HtrII molecules are complexed with Alexa 488-labeled transducer molecules. The expected value assuming equal labeling efficiencies for both dyes is 50%, thus corroborating coreconstitution of at least 2 *Np*SRII/*Np*HtrII heterodimers into the NLPs. Furthermore, from the autocorrelation curves, a diffusion constant of 33 ± 4 $\mu m^2/s$ was obtained for the *Np*SRII/*Np*HtrII complex reconstituted into nanodiscs. This corresponds to a hydrodynamic radius of 7.5 ± 0.8 nm, in good agreement with the size of the complex observed in size exclusion chromatography.

To gain further information about the composition of the *Np*SRII/*Np*HtrII/NLP complexes, we applied time-lapse single molecule (SM) imaging. This technique takes advantage of the quantal photobleaching of fluorescent molecules over time to resolve two or more fluorophores in the $x-y$ plane separated by distances in the range of a few nm.[59,60] By recording a series of images and subsequent analysis of the bleaching performance, the number of emitters hidden in one particle can be identified by a stepwise bleaching behavior.

The same NLP fraction that has been taken for the FCCS experiments was also used for SM imaging. To reduce background, emitters adsorbed at the coverslip surface were excited in total internal reflection fluorescence (TIRF) mode. The concentration was low enough to distinguish single particles in one frame (Figure 7C). A surface plot of the same frame demonstrates the difference in integrated intensity (Figure 7D), corresponding to a two-emitter particle and a one-emitter particle. By application of a modified 2D Gaussian fit, the centers of fluorescence could be determined from the fluorescence image of single emitters.[61] In our experiments, the localization precision of this assignment was in the range of 100−150 Å (data not shown) what is not sufficient to optically resolve two fluorescent molecules within a 140 Å diameter NLP assembly. Though, by time-dependent fluorescent analysis of single particles, the bleaching kinetics gives information about the number of fluorescent molecules in one particle. Each single fluorophore is supposed to switch off in a single step. We found that most of the *Np*HtrII/*Np*SRII/NLP complexes investigated contain 1 or 2 single emitters as evidenced by distinct intensity levels and single-step transitions between the fluorescence levels. Figure 7E shows the sequential photobleaching of a complex comprised of two *Np*HtrII molecules labeled with Alexa 488. Figure 7F shows a time course from an Alexa 594-tagged *Np*HtrII/*Np*SRII/NLP assembly. Again, the bleaching is a two-step process evidencing the presence of two *Np*HtrII-emitters. Hence, SM imaging analysis confirms the reconstitution of the *Np*HtrII/*Np*SRII complex in NLP corresponding to the expected 2:2:1 stoichiometry of an *Np*HtrII/*Np*SRII/NLP assembly.

Flash Photolysis Experiments on NpSRII/NpHtrII/NLP Assemblies. The physiological response of the *Np*SRII/*Np*HtrII complex, i.e., signal transduction, is triggered by the light-induced reaction cycle (photocycle) of *Np*SRII.[8] It has been shown that the external conditions may considerably influence the photocycle kinetics.[8,62−65] Therefore, we performed flash photolysis experiments to check whether reconstitution of *Np*SRII/*Np*HtrII into NLPs could affect the photocycle of the receptor. The light-activated transient absorption changes of *Np*SRII were measured at three different indicative wavelengths. The recovery of the ground state was recorded at 500 nm, whereas the decay of the M-intermediate was followed at 400 nm. The trace at 550 nm represents the formation and decay of the final red-shifted O-intermediate.

Figure 8 shows the photocycle kinetics of the complex in NLPs and in the PML-reconstituted state at salt concentrations

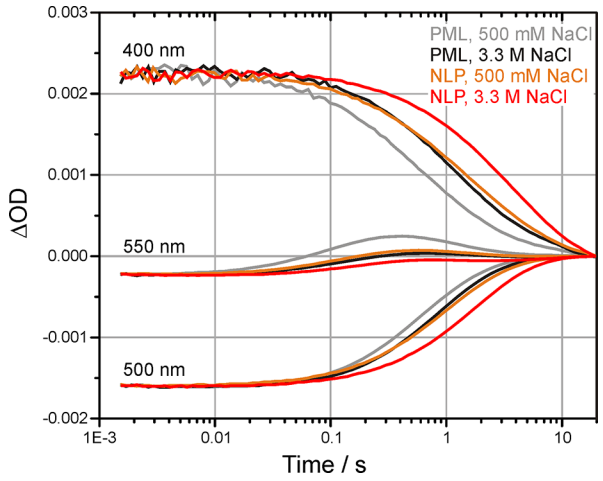

Figure 8. Flash photolysis of the NpSRII/NpHtrII-N351R1 complex. Transient optical absorption changes for the complex reconstituted in NLPs at 500 mM NaCl salt concentration (orange traces) and with 3.3 M NaCl (red), compared to the data obtained for the same complex in PML (500 mM NaCl, gray; 3.3 M NaCl, black). Transient absorption changes are recorded at 25 °C at wavelengths characteristic for the sensory rhodopsin photocycle: 400 nm (M state), 500 nm (ground state), and 550 nm (O state). The traces are normalized to the amplitudes in the time window t = 2−3 ms.

of 500 mM and 3.3 M NaCl for the second half of the photocycle. The photocycle of *Np*SRII in the NLP-reconstituted samples is significantly slower compared to the PML-reconstituted samples. Furthermore, for both types of preparations increasing the salt concentration leads to further retardation of the photocycle kinetics. The major effect is observed for the M-decay that is slowed down for the NLP compared to the PML samples by factors of 2 and 3 at 500 mM and 3.3 M salt concentration, respectively. The turnover rates are less affected and consequently the transient amounts of the O-intermediate are reduced. Interestingly, the photocycles of the PML sample at 3.3 M NaCl and of the NLP-reconstituted complex at 500 mM salt concentration exhibit very similar lifetimes of the respective intermediates, although the M decay and the ground state recovery show slightly different kinetics.

Above we have shown that the *Np*SRII/*Np*HtrII complex assembles in NLPs as a 2:2 complex (see Figures 6 and 7). Thus, it can be speculated that the observed "acceleration" of the photocycle of the PML-reconstituted *Np*SRII/*Np*HtrII complex compared to that of the NLP-reconstituted sample is caused by interactions of photoreceptor molecules immobilized within the arrays formed in the purple membrane lipids. An analogous effect of clustering on the photocycle kinetics has been shown in case of the BR preparations, although in this case aggregation decelerates the photocycle.[66] Nevertheless, a previous comparison between the photocycle of *Np*SRII in complex with the full-length transducer and bound to a transducer construct truncated at position 157 ($NpHtrII_{157}$) revealed slower kinetics (e.g., the M decay is slowed down by a factor of 2) for the full-length construct,[27] indicating a direct influence of the cytoplasmic domain of *Np*HtrII. Consequently,

dx.doi.org/10.1021/bi501160q | *Biochemistry* 2015, 54, 349−362

another explanation for our observations could be the absence of interdimer contacts for the transducer in NLPs that modulates the *Np*SRII photocycle, speaking in favor of the notion that transducer and receptor are conformationally coupled. Similar coupling has been proposed for the closely related SRI/HtrI photoreceptor complex from *H. salinarum*, where the influence of mutations in HtrI on the Schiff base connectivity in SRI suggested "that the SRI subunit and adjacent parts of HtrI, including the membrane proximal portion of the HAMP domain, function as a single unit that undergoes concerted conformational transitions".[67] Nevertheless, the reason for the observed acceleration is not yet clear and remains in the focus of our current and future studies.

Spin Label Mobility and Inter Spin Distances of NpSRII/NpHtrII in NLPs. In order to investigate the effect of the reconstitution of the receptor/transducer complex in NLPs on the dynamic behavior of the transducer and on interspin distances, we performed cw and DEER EPR experiments on a selected spin label mutant (*Np*SRII/*Np*HtrII-N351R1) in the transducer tip region. The results are shown in Figure 9. The

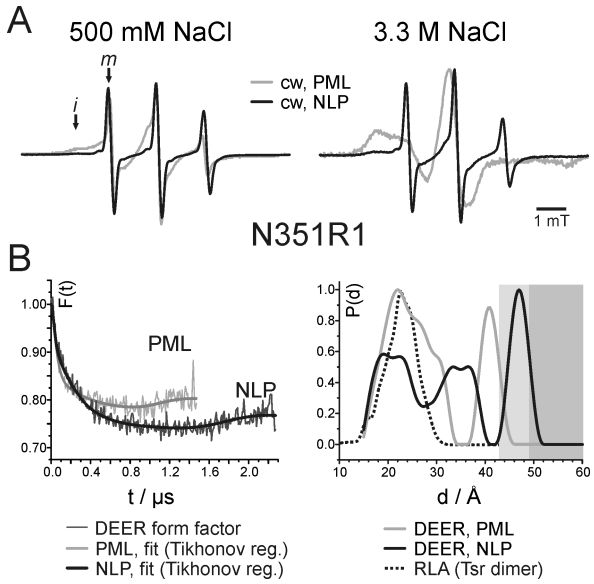

Figure 9. Spin label mobility and interspin distances for *Np*SRII/*Np*HtrII-N351R1/NLP assemblies. (A) Amplitude normalized cw RT EPR spectra recorded at 500 mM (left panel) and 3.3 M NaCl (right panel), compared to the spectra of *Np*SRII/*Np*HtrII-N351R1 reconstituted in PML (gray spectra). (B) DEER distance analysis. DEER background corrected dipolar evolution data (left column) and resulting distance distributions (right column, black solid lines) obtained by Tikhonov regularization of the data shown on the left. The gray dotted and black dashed lines represents the results of a RLA on the Tsr structural model (see Figures 1B,C and 5C).

cw RT EPR spectra recorded at 500 mM and 3.3 M salt concentration in comparison to the corresponding spectra of the PML reconstituted complex (Figure 9A) seem to reflect strong shifts of the conformational equilibrium due to reconstitution in NLPs toward the more mobile state in both cases, being most obvious at physiological salt concentration. Closer inspection of the spectra reveals also an increased (isotropic) hyperfine-splitting, a_{iso}, indicating different spin label environments in the PML- and NLP reconstituted state of the complex. In connection with the extreme increase of spin label side chain mobility even at high salt concentration this indicates almost complete loss of tertiary contacts, thus indicating that in a 2:2 *Np*SRII/*Np*HtrII complex in nanodiscs the two transducer molecules are mostly dissociated at the cytoplasmic tip even at high salt concentration.

DEER interspin distance measurements on a NLP reconstituted sample give a modulated DEER signal that can be analyzed in terms of a distance distribution (Figure 9B) that is characterized by maxima at ~20, 35, and 48 Å, thus indicating multiple spin spin interactions in the sample what seems to contradict the results of the cw RT measurements (see above). We interpret this finding as caused by oligomerization upon freezing. Comparison of the form factors and distance distributions obtained with the PML- (Figure 9B, gray) and NLP-reconstituted (Figure 9B, black) samples shows clear differences, indicating different modes of oligomerization in the two samples. Indeed, Cryo-electron microscopy data for chemoreceptor arrays revealed that in the absence of the CheA/CheW baseplate (when Tsr is overproduced in the cells) the receptors can interact radially and axially.[68]

CONCLUSIONS

In the present study we show that the cytoplasmic tip domain of *Np*HtrII is engaged in a "two-state" equilibrium between a dynamic and a compact conformation. Analogous to what has been observed for the first HAMP domain of the transducer,[13,24,40] in the dynamic conformation spin label side chains at positions close to the cytoplasmic tip of the four-helix bundle are characterized by high mobility, typical for labels bound to flexible loop regions or to partially unfolded structures. In the compact conformation all studied sites appear to be strongly immobilized. Interestingly, previously published biochemical and in vivo data[24] and our own observations (to be published) indicate opposing conformational changes and thus dynamics in HAMP2 compared to HAMP1. Consequently, we support a model where the whole transducer protein is involved in a two-state equilibrium and where possibly consecutive domains with different dynamics relay the signal to the kinase CheA.

Furthermore, interspin distance measurements provide the first experimental evidence that archaeal photoreceptor/-transducer complexes form trimers-of-dimers or higher-order assemblies analogous to methyl-accepting chemotaxis proteins, again stressing conservation of the overall mechanistic principles underlying the archaeal phototaxis and bacterial chemotaxis systems. Interestingly, interspin distance measurements on isolated 2:2 photoreceptor/transducer complexes in NLPs revealed spin−spin interactions beyond those expected for two labels in a transducer dimer, although characterization of the SRII/HtrII/NLP preparations by fluorescence spectroscopy and microscopy gave clear indications for the presence of not more than one transducer dimer in the NLPs. We speculate that the mutual affinity of the transducer tips is high enough to lead to the assembly of several *Np*SRII/*Np*HtrII/NLPs in solution at the sample concentrations used for the EPR experiments, whereas in the fluorescence spectroscopy experiments significantly lower concentrations have been used. Thus, our results reveal that formation of ordered photoreceptor/-transducer clusters is independent of the presence of the cytoplasmic components CheA/CheW like it has been observed also for bacterial chemoreceptor arrays.[45,69−71]

Finally, photocycle measurements of *Np*SRII in complex with the full-length transducer and bound to a transducer construct truncated at position 157 (*Np*HtrII$_{157}$) in NLPs revealed significant differences in the photocycle kinetics for the full-

dx.doi.org/10.1021/bi501160q | *Biochemistry* 2015, 54, 349−362

length construct, indicating a tight coupling of the two proteins in the transmembrane region and also a direct influence of the cytoplasmic domain of *Np*HtrII. With regard to the mechanism of signal transduction this suggests that activation/deactivation signals are communicated in both directions along the elongated rod-like structure and also back to SRII.

In summary, the data presented in this paper reveal the presence of a two-state equilibrium between a dynamic and a more compact state also at the kinase-interacting tip domain, thus suggesting that the whole transducer protein might be involved in such equilibrium. Furthermore, our results show a two-dimensional clustering of SRII/HtrII complexes in—most likely—trimers of dimers in the membrane, like it is well established for chemoreceptors, Taken together, our findings provide further evidence for the close kinship of photo- and chemotaxis, and that changes in dynamics are the language of signal transfer in both systems.[13,72]

■ ASSOCIATED CONTENT

Supporting Information

Spectra for the lipid dilution experiment and full thermodynamic analysis of temperature dependent spectra. This material is available free of charge via the Internet at http://pubs.acs.org.

■ AUTHOR INFORMATION

Corresponding Author

*E-mail: jklare@uos.de. Tel: +49 541 969 2664. Fax: +49 541 969 2656.

Author Contributions

§I.O.-G. and N.V. contributed equally.

Funding

This work was supported by the Volkswagen-Stiftung (N. V.), the Deutsche Forschungsgemeinschaft (SFB 944/P10 to J.P.K., H.-J.S. and J.P.; Grant BU 2288/1-1 to K. B.B.), and the Cultural Office of the Embassy of the Arab Republic of Egypt to W.M.

Notes

The authors declare no competing financial interest.

■ ACKNOWLEDGMENTS

The authors thank Dr. Armen Mulkidjanian for helpful discussions.

■ ABBREVIATIONS

BR, bacteriorhopsin; cw, continuous wave; DDM, *n*-dodecyl-β-D-maltoside; DEER, double electron electron resonance; EPR, electron paramagnetic resonance; FCCS, fluorescence cross-correlation spectroscopy; HR, halorhodopsin; HtrII, halobacterial transducer of rhodopsin II; MTSSL, 1-oxyl-2,2,5,5-tetramethylpyrroline-3-methyl) methanethiosulfonate spin label; NLPs, nanolipoprotein particles; PML, purple membrane lipids; RLA, rotamer library approach; SEC, size exclusion chromatography; SDSL, site-directed spin labeling; SRII, sensory rhodopsin II; TEM, transmission electron microscopy; TIRF, total internal reflection fluorescence

■ REFERENCES

(1) Klare, J. P., Chizhov, I., and Engelhard, M. (2007) Microbial Rhodopsins: Scaffolds for Ion Pumps, Channels, and Sensors. *Results Probl. Cell Differ. 45*, 73−122.

(2) Hoff, W. D., Jung, K. H., and Spudich, J. L. (1997) Molecular mechanism of photosignaling by archaeal sensory rhodopsins. *Annu. Rev. Biophys. Biomol. Struct. 26*, 223−258.

(3) Spudich, J. L., Yang, C. S., Jung, K. H., and Spudich, E. N. (2000) Retinylidene proteins: structures and functions from archaea to humans. *Annu. Rev. Cell. Dev. Biol. 16*, 365−392.

(4) Klare, J. P., Gordeliy, V. I., Labahn, J., Büldt, G., Steinhoff, H.-J., and Engelhard, M. (2004) The archaeal sensory rhodopsin II/transducer complex: a model for transmembrane signal transfer. *FEBS Lett. 564*, 219−224.

(5) Royant, A., Nollert, P., Edman, K., Neutze, R., Landau, E. M., Pebay-Peyroula, E., and Navarro, J. (2001) X-ray structure of sensory rhodopsin II at 2.1-A resolution. *Proc. Natl. Acad. Sci. U.S.A. 98*, 10131−10136.

(6) Luecke, H., Schobert, B., Lanyi, J. K., Spudich, E. N., and Spudich, J. L. (2001) Crystal Structure of Sensory Rhodopsin II at 2.4 Å: Insights into Color Tuning and Transducer Interaction. *Science 293*, 1499−1503.

(7) Gordeliy, V. I., Labahn, J., Moukhametzianov, R., Efremov, R., Granzin, J., Schlesinger, R., Büldt, G., Savopol, T., Scheidig, A. J., Klare, J. P., and Engelhard, M. (2002) Molecular basis of transmembrane signalling by sensory rhodopsin II-transducer complex. *Nature 419*, 484−487.

(8) Chizhov, I., Schmies, G., Seidel, R., Sydor, J. R., Lüttenberg, B., and Engelhard, M. (1998) The photophobic receptor from Natronobacterium pharaonis: temperature and pH dependencies of the photocycle of sensory rhodopsin II. *Biophys. J. 75*, 999−1009.

(9) Aravind, L., and Ponting, C. P. (1999) The cytoplasmic helical linker domain of receptor histidine kinase and methyl-accepting proteins is common to many prokaryotic signalling proteins. *FEMS Microbiol. Lett. 176*, 111−116.

(10) Hulko, M., Berndt, F., Gruber, M., Linder, J. U., Truffault, V., Schultz, A., Martin, J., Schultz, J. E., Lupas, A. N., and Coles, M. (2006) The HAMP Domain Structure Implies Helix Rotation in Transmembrane Signaling. *Cell 126*, 929−940.

(11) Wegener, A. A., Klare, J. P., Engelhard, M., and Steinhoff, H.-J. (2001) Structural insights into the early steps of receptor-transducer signal transfer in archaeal phototaxis. *EMBO J. 20*, 5312−5319.

(12) Wegener, A. A., Chizhov, I., Engelhard, M., and Steinhoff, H.-J. (2000) Time-resolved detection of transient movement of Helix F in spin-labelled Pharaonis sensory rhodopsin II. *J. Mol. Biol. 301*, 881−891.

(13) Doebber, M. A., Bordignon, E., Klare, J. P., Holterhues, J., Martell, S., Mennes, N., Li, L., Engelhard, M., and Steinhoff, H.-J. (2008) Salt-driven equilibrium between two conformations in the HAMP domain from Natronomonas pharaonis, the language of signal transfer? *J. Biol. Chem. 283*, 28691−28701.

(14) Klare, J. P., Bordignon, E., Engelhard, M., and Steinhoff, H.-J. (2011) Transmembrane signal transduction in archaeal phototaxis: The sensory rhodopsin II-transducer complex studied by electron paramagnetic resonance spectroscopy. *Eur. J. Cell Biol. 90*, 731−739.

(15) Khursigara, C. M., Wu, X., Zhang, P., Lefman, J., and Subramaniam, S. (2008) Role of HAMP domains in chemotaxis signaling by bacterial chemoreceptors. *Proc. Natl. Acad. Sci. U.S.A. 105*, 16555−16560.

(16) Kim, K. K., Yokota, H., and Kim, S. H. (1999) Four-helical-bundle structure of the cytoplasmic domain of a serine chemotaxis receptor. *Nature 400*, 787−792.

(17) Ames, P., Studdert, C. A., Reiser, R. H., and Parkinson, J. S. (2002) Collaborative signaling by mixed chemoreceptor teams in Escherichia coli. *Proc. Natl. Acad. Sci. U.S.A. 99*, 7060−7065.

(18) Studdert, C. A., and Parkinson, J. S. (2004) Crosslinking snapshots of bacterial chemoreceptor squads. *Proc. Natl. Acad. Sci. U.S.A. 101*, 2117−2122.

(19) Hazelbauer, G. L., Falke, J. J., and Parkinson, J. S. (2008) Bacterial chemoreceptors: high-performance signaling in networked arrays. *Trends Biochem. Sci. 33*, 9−19.

(20) Trivedi, V. D., and Spudich, J. L. (2003) Photostimulation of a Sensory Rhodopsin II/HtrII/Tsr Fusion Chimera Activates CheA-

Autophosphorylation and CheY-Phosphotransfer in Vitro. *Biochem. 42*, 13887−13892.
(21) Boldog, T., Grimme, S., Li, M., Sligar, S. G., and Hazelbauer, G. L. (2006) Nanodiscs separate chemoreceptor oligomeric states and reveal their signaling properties. *Proc. Natl. Acad. Sci. U.S.A. 103*, 11509−11514.
(22) Amin, D. N., and Hazelbauer, G. L. (2010) The Chemoreceptor Dimer is the Unit of Conformational Coupling and Transmembrane Signaling. *J. Bacteriol. 192*, 1193−1200.
(23) Li, M., and Hazelbauer, G. L. (2011) Core unit of chemotaxis signaling complexes. *Proc. Natl. Acad. Sci. U.S.A. 108*, 9390−9395.
(24) Wang, J., Sasaki, J., Tsai, A. L., and Spudich, J. L. (2012) HAMP Signal Relay Mechanism in a Sensory Rhodopsin-Transducer Complex. *J. Biol. Chem. 287*, 21316−21325.
(25) Hohenfeld, I. P., Wegener, A. A., and Engelhard, M. (1999) Purification of Histidine tagged bacteriorhodopsin, pharaonis halorhodopsin and pharaonis sensory rhodopsin II functionally expressed in Escherichia coli. *FEBS Lett. 442*, 198−202.
(26) Shimono, K., Iwamoto, M., Sumi, M., and Kamo, N. (1997) Functional expression of pharaonis phoborhodopsin in Escherichia coli. *FEBS Lett. 420*, 54−56.
(27) Mennes, N., Klare, J. P., Chizhov, I., Seidel, R., Schlesinger, R., and Engelhard, M. (2007) Expression of the halobacterial transducer protein HtrII from Natronomonas pharaonis in Escherichia coli. *FEBS Lett. 581*, 1487−1494.
(28) Jonas, A. (1986) Reconstitution of high-density lipoproteins. *Methods Enzymol. 128*, 553−582.
(29) Steinhoff, H.-J., Radzwill, N., Thevis, W., Lenz, V., Brandenburg, W., Antson, A., Dodson, G., and Vollmer, A. (1997) Determination of interspin distances between spin labels attached to insulin: comparison of electron paramagnetic resonance data with the X- ray structure. *Biophys. J. 73*, 3287−3298.
(30) Pannier, M., Veit, S., Godt, A., Jeschke, G., and Spiess, H. W. (2000) Dead-Time Free Measurement of Dipole-Dipole Interactions between Electron Spins. *J. Magn. Reson. 142*, 331−340.
(31) Jeschke, G., and Polyhach, Y. (2007) Distance Measurements on Spin-Labelled Biomacromolecules by Pulsed Electron Paramagnetic Resonance. *Phys. Chem. Chem. Phys. 9*, 1895−1910.
(32) Jeschke, G., Chechik, V., Ionita, V., Godt, A., Zimmermann, H., Banham, J., Timmel, C. R., Hilger, D., and Jung, H. (2006) DeerAnalysis2006 - A Comprehensive Software Package for Analyzing Pulsed ELDOR Data. *Appl. Magn. Reson. 30*, 473−498.
(33) Freed, J. H. (1976) Theory of Slow Tumbling ESR Spectra for Nitroxides, in *Spin Labeling: Theory and Applications* (Berliner, L. J., Ed.) pp 53−132, Academic Press, New York.
(34) Polyhach, Y., Bordignon, E., and Jeschke, G. (2011) Rotamer libraries of spin labelled cysteines for protein studies. *Phys. Chem. Chem. Phys. 13*, 2356−2366.
(35) Mackerell, A. D., Jr., Feig, M., and Brooks, C. L., III (2004) Extending the treatment of backbone energetics in protein force fields: Limitations of gas-phase quantum mechanics in reproducing protein conformational distributions in molecular dynamics simulations. *J. Comput. Chem. 25*, 1400−1415.
(36) Holterhues, J., Bordignon, E., D.Klose, D., Rickert, C., Klare, J. P., Martell, S., Li, L., Engelhard, M., and Steinhoff, H.-J. (2011) The Signal Transfer from the Receptor NpSRII to the Transducer NpHtrII Is Not Hampered by the D75N Mutation. *Biophys. J. 100*, 2275−2282.
(37) Mchaourab, H. S., Lietzow, M. A., Hideg, K., and Hubbell, W. L. (1996) Motion of Spin-Labeled Side Chains in T4 Lysozyme. Correlation with Protein Structure and Dynamics. *Biochemistry 35*, 7692−7704.
(38) Hubbell, W. L., Cafiso, D. S., and Altenbach, C. (2000) Identifying conformational changes with site-directed spin labeling. *Nat. Struct. Biol. 7*, 735−739.
(39) Langen, R., Oh, K. J., Cascio, D., and Hubbell, W. L. (2000) Crystal Structures of Spin Labeled T4 Lysozyme Mutants: Implications for the Interpretation of EPR Spectra in Terms of Structure. *Biochem. 39*, 8396−8405.
(40) Bordignon, E., Klare, J. P., Doebber, M., Wegener, A. A., Martell, S., Engelhard, M., and Steinhoff, H. J. (2005) Structural Analysis of a HAMP Domain: The Linker Region of the Phototransducer in Complex with Sensory Rhodopsin II. *J. Biol. Chem. 280*, 38767−38775.
(41) Sasaki, J., Phillips, B. J., Chen, X., Van Eps, N., Tsai, A.-L., Hubbell, W. L., and Spudich, J. L. (2007) Different Dark Conformations Function in Color-Sensitive Photosignaling by the Sensory Rhodopsin I-HtrI Complex. *Biophys. J. 92*, 4045−4053.
(42) Jung, K.-H., and Spudich, J. L. (1998) Suppressor Mutation Analysis of the Sensory Rhodopsin I - Transducer Complex: Insights into the Color-Sensing Mechanism. *J. Bacteriol. 180*, 2033−2042.
(43) Soliman, G. S. H., and Truper, H. G. (1982) *Halobacterium-Pharaonis* Sp-Nov, a New, Extremely Haloalkaliphilic Archaebacterium with Low Magnesium Requirement. *Zentralblatt fur Bakteriologie Mikrobiologie und Hygiene I Abteilung Originale C-Allgemeine Angewandte und Okologische Mikrobiologie 3*, 318−329.
(44) Rodriguez, V. (1993) Introduction to saline environments. In *The Biology of Halophilic Bacteria* (Vreeland, R. H., Hochstein, L. I., Eds.) pp 1−23, CRC Press, Boca Raton, FL.
(45) Lide, D. R. (2007) *CRC Handbook of Chemistry and Physics*, 88th ed. (Internet Version 2008) CRC Press/Taylor and Francis, Boca Raton, FL.
(46) Steinhoff, H.-J., Lieutnant, K., and Schlitter, J. (1989) Residual motion of hemoglobin-bound spin labels as a probe for protein dynamics. *Z. Naturforsch. C 44*, 280−288.
(47) Kentner, D., Thiem, S., Hildenbeutel, M., and Sourjik, V. (2006) Determinants of chemoreceptor cluster formation in Escherichia coli. *Mol. Microbiol. 61*, 407−417.
(48) Jonas, A., Kezdy, K. E., and Wald, J. H. (1989) Defined apolipoprotein A-I conformations in reconstituted high density lipoprotein discs. *J. Biol. Chem. 264*, 4818−4824.
(49) Jonas, A., Wald, J. H., Toohill, K. L., Krul, E. S., and Kezdy, K. E. (1990) Apolipoprotein A-I structure and lipid properties in homogeneous, reconstituted spherical and discoidal high density lipoproteins. *J. Biol. Chem. 265*, 22123−22129.
(50) Carlson, J. W., Jonas, A., and Sligar, S. G. (1997) Imaging and manipulation of high-density lipoproteins. *Biophys. J. 73*, 1184−1189.
(51) Eisenberg, S. (1984) High density lipoprotein metabolism. *J. Lipid Res. 25*, 1017−1058.
(52) Blanchette, C. D., Law, R., Benner, W. H., Pesavento, J. B., Cappuccio, J. A., Walsworth, V., Kuhn, E. A., Corzett, M., Chromy, B. A., Segelke, B. W., Coleman, M. A., Bench, G., Hoeprich, P. D., and Sulchek, T. A. (2008) Quantifying size distributions of nano-lipoprotein particles with single-particle analysis and molecular dynamic simulations. *J. Lipid Res. 49*, 1420−1430.
(53) Li, L., Chen, J., Mishra, V. K., Kurtz, J. A., Cao, D., Klon, A. E., Harvey, S. C., Anantharamaiah, G. M., and Segrest, J. P. (2004) Double belt structure of discoidal high density lipoproteins: molecular basis for size heterogeneity. *J. Mol. Biol. 343*, 1293−1311.
(54) Schwille, P., Meyer-Almes, F. J., and Rigler, R. (1997) Dual-color fluorescence cross-correlation spectroscopy for multicomponent diffusional analysis in solution. *Biophys. J. 72*, 1878−1886.
(55) Haustein, E., and Schwille, P. (2004) Single-molecule spectroscopic methods. *Curr. Opin. Struct. Biol. 14*, 531−540.
(56) Kim, S. A., Heinze, K. G., Waxham, M. N., and Schwille, P. (2004) Intracellular calmodulin availability accessed with two-photon cross-correlation. *Proc. Natl. Acad. Sci. U.S.A. 101*, 105−110.
(57) Heinze, K. G., Rarbach, M., Jahnz, M., and Schwille, P. (2002) Two-photon fluorescence coincidence analysis: rapid measurements of enzyme kinetics. *Biophys. J. 83*, 1671−1681.
(58) Bacia, K., Kim, S. A., and Schwille, P. (2006) Fluorescence cross-correlation spectroscopy in living cells. *Nat. Methods 3*, 83−89.
(59) Gordon, M. P., Ha, T., and Selvin, P. R. (2004) Single-molecule high-resolution imaging with photobleaching. *Proc. Natl. Acad. Sci. U.S.A. 101*, 6462−6465.
(60) Arant, R. J., and Ulbrich, M. H. (2014) Deciphering the subunit composition of multimeric proteins by counting photobleaching steps. *ChemPhysChem 15*, 600−605.

(61) Thompson, R. E., Larson, D. R., and Webb, W. W. (2002) Precise nanometer localization analysis for individual fluorescent probes. *Biophys. J. 82*, 2775−2783.
(62) Schmies, G., Lüttenberg, B., Chizhov, I., Engelhard, M., Becker, A., and Bamberg, E. (2000) Sensory rhodopsin II from the haloalkaliphilic natronobacterium pharaonis: light-activated proton transfer reactions. *Biophys. J. 78*, 967−976.
(63) Imamoto, Y., Shichida, Y., Hirayama, J., Tomioka, H., Kamo, N., and Yoshizawa, T. (1992) Nanosecond Laser Photolysis of Phoborhodopsin from Natronobacterium-Pharaonis Appearance of Kl and L Intermediates in the Photocycle at Room-Temperature. *Photochem. Photobiol. 56*, 1129−1134.
(64) Kamo, N., Shimono, K., Iwamoto, M., and Sudo, Y. (2001) Photochemistry and photoinduced proton-transfer by pharaonis phoborhodopsin. *Biochem. (Moscow) 66*, 1277−1282.
(65) Klare, J. P., Bordignon, E., Doebber, M., Fitter, J., Kriegsmann, J., Chizhov, I., Steinhoff, H.-J., and Engelhard, M. (2006) Effects of Solubilization on the Structure and Function of the Sensory Rhodopsin II/Transducer Complex. *J. Mol. Biol. 356*, 1207−1221.
(66) Grzesiek, S., and Dencher, N. A. (1988) Monomeric and Aggregated Bacteriorhodopsin: Single-Turnover Proton Transport Stoichiometry and Photochemistry. *Proc. Natl. Acad. Sci. U.S.A. 85*, 9509−9513.
(67) Sineshchekov, O. A., Sasaki, J., Phillips, B. J., and Spudich, J. L. (2008) A Schiff base connectivity switch in sensory rhodopsin signaling. *Proc. Natl. Acad. Sci. U.S.A. 105*, 16159−16164.
(68) Zhang, P., Khursigara, C. M., Hartnell, L. M., and Subramaniam, S. (2007) Direct visualization of Escherichia coli chemotaxis receptor arrays using cryo-electron microscopy. *Proc. Natl. Acad. Sci. U.S.A. 104*, 3777−3781.
(69) Lefman, J., Zhang, P., Hirai, T., Weis, R. M., Juliani, J., Bliss, D., Kessel, M., Bos, E., Peters, P. J., and Subramaniam, S. (2004) Three-dimensional electron microscopic imaging of membrane invaginations in Escherichia coli overproducing the chemotaxis receptor Tsr. *J. Bacteriol. 186*, 5052−5061.
(70) McAndrew, R. S., Ellis, E. A., Manson, M. D., and Holzenburg, A. (2004) TEM analysis of chemoreceptor arrays in native membranes of *E. coli*. *Microsc. Microanal. 10*, 416−417.
(71) Zhang, P., Bos, E., Heymann, J., Gnaegi, H., Kessel, M., Peters, P. J., and Subramaniam, S. (2004) Direct visualization of receptor arrays in frozen-hydrated sections and plunge-frozen specimens of E. coli engineered to overproduce the chemotaxis receptor Tsr. *J. Microsc. 216*, 76−83.
(72) Klose, D., Voskoboynikova, N., Orban-Glass, I., Rickert, C., Engelhard, M., Klare, J. P., and Steinhoff, H.-J. (2014) Light-induced switching of HAMP domain conformation and dynamics revealed by time-resolved EPR spectroscopy. *FEBS Lett. 588*, 3970−3976.